

PAPER



Cite this: *Phys. Chem. Chem. Phys.*,
2018, 20, 26315

Dynamics and kinetics of the reaction $\text{OH} + \text{H}_2\text{S} \rightarrow \text{H}_2\text{O} + \text{SH}$ on an accurate potential energy surface

Leilei Ping,^{†ab} Yongfa Zhu,^{id†ac} Anyang Li,^d Hongwei Song,^{id*} Yong Li^{*b} and
Minghui Yang^{ida}

The dynamics and kinetics of the prototypical hydrogen abstraction reaction $\text{OH} + \text{H}_2\text{S} \rightarrow \text{H}_2\text{O} + \text{SH}$ were studied using the quasi-classical trajectory approach on a new accurate *ab initio* potential energy surface (PES) for the ground electronic state. The PES was developed by fitting 82 680 *ab initio* points at the level of UCCSD(T)-F12a/aug-cc-pVTZ using the fundamental invariant-neural network method. On one hand, excitation of either the symmetric stretching mode or the asymmetric stretching mode of the reactant H_2S almost equivalently enhances the reaction. The promotional effect of exciting the bending mode of H_2S is not as strong as exciting the stretching modes while it increases with the collision energy. On the other hand, the calculated vibrational state distribution of the product H_2O based on the normal mode analysis method agrees reasonably well with the earlier experimental result, which was rationalized by the underlying reaction mechanisms. In addition, the rate constants of the reaction have a non-Arrhenius temperature dependence.

Received 18th August 2018,
Accepted 18th September 2018

DOI: 10.1039/c8cp05276j

rsc.li/pccp

I. Introduction

Hydrogen sulfide (H_2S) plays an important role in chemical processes associated with air pollution, acid rain and climate change.^{1–5} The hydrogen abstraction reaction between OH and H_2S is a key step in the chains of the oxidation and ignition of H_2S .^{6–8} Due to its importance in the troposphere and stratosphere, the kinetics of the reaction has been widely studied both experimentally^{9–15} and theoretically^{16–19} in the past several decades. The rate constants were measured to be about $(3.1\text{--}5.7) \times 10^{-12} \text{ cm}^3 \text{ molecule}^{-1} \text{ s}^{-1}$ at 298 K and had an unusual temperature dependence at lower and higher temperatures, indicating the existence of a non-Arrhenius behavior.^{9–15,20–23}

Ellington and Truhlar¹⁸ argued that the unusual temperature dependence arises from a dynamical bottleneck at an energy below that of the reactants by direct dynamics with the M06-2X density functional using the MG3S basis set. In contrast, there have been very few dynamics investigations on the reaction. To the best of our

knowledge, only Butkovskaya and Setser²⁴ reported nascent vibrational distributions of the product molecules H_2O and HDO formed from the room-temperature reactions of OH and OD radicals with H_2S , in which the infrared chemiluminescence of the product molecules was recorded by using a fast-flow reactor with a Fourier transform spectrometer.

Theoretically, the interaction of H_2S with OH has been investigated using various first-principle methods.^{16,19,25–27} Impressively, Alday *et al.*²⁶ predicted that H_2S forms a strong two-center three-electron hemibond with a free radical OH and the hemibond complex has much stronger binding energy than that involving H_2O by performing *ab initio* calculations at the level of UCCSD(T)-F12a/aug-cc-pVTZ. The hemibond complex was thought to have an important impact on the reaction between OH and H_2S . Very recently, Tang *et al.*²⁷ investigated the stationary points along the minimum energy path of the reaction using the “gold standard” CCSD(T) method together with the Dunning’s aug-cc-pVXZ (up to 5Z) basis sets. In both the entrance and exit channels, they reported two hydrogen-bonded complexes and one hemibonded isomer, with one of the hydrogen-bonded complexes being lowest-lying. The classical barrier height was determined to be only 0.11 kcal mol^{−1} with aug-cc-pV5Z single point energies at the aug-cc-pVQZ geometries.

Although the stationary points on the potential energy surface (PES) of the hydrogen abstraction reaction $\text{OH} + \text{H}_2\text{S} \rightarrow \text{H}_2\text{O} + \text{SH}$ have been thoroughly studied using high-level *ab initio* methods, no global PES has been reported to date.

^a State Key Laboratory of Magnetic Resonance and Atomic and Molecular Physics, Wuhan Institute of Physics and Mathematics, Chinese Academy of Sciences, Wuhan 430071, China. E-mail: hwsong@wipm.ac.cn

^b College of Physical Science and Technology, Huazhong Normal University, Wuhan 430079, China. E-mail: yongli@mail.ccnu.edu.cn

^c University of Chinese Academy of Sciences, Beijing 100049, China

^d College of Chemistry and Materials Science, Northwest University, Xi’an, 710127, China

[†] L. Ping and Y. Zhu contributed equally to this work.

In this work, we construct a global, full-dimensional ground-state reactive PES for the $\text{OH} + \text{H}_2\text{S} \rightarrow \text{H}_2\text{O} + \text{SH}$ reaction. The PES is fitted using the fundamental invariant-neural network (FI-NN) method²⁸ based on 82 680 *ab initio* points at the level of UCCSD(T)-F12a/aug-cc-pVTZ.^{29,30} The quasi-classical trajectory (QCT) method³¹ is then employed to study the dynamics and kinetics of the reaction, unveiling the mode specificity, the product energy partitioning and the non-Arrhenius behavior in the reaction. The paper is organized as follows. Section II outlines the details of the *ab initio* potential energy surface, followed by a very brief introduction of the quasi-classical trajectory method and the normal mode analysis (NMA) method in Section III. The results and discussion are given in Section IV. We conclude in Section V.

II. Potential energy surface

To construct an accurate PES of a polyatomic reaction, it is of key importance to balance the accuracy of the *ab initio* methods with the associated computational cost. This generally can be achieved by performing test calculations of the geometries and energies of stationary points along the reaction path with varying levels of *ab initio* methods and basis sets. Fortunately, as aforementioned, Tang *et al.*²⁷ studied the stationary points on the PES of the $\text{OH} + \text{H}_2\text{S} \rightarrow \text{H}_2\text{O} + \text{SH}$ reaction using the CCSD(T) method with the basis set up to aug-cc-pV(5+d)Z. They concluded that the stationary point energies are not sensitive to the additional d functions on the S atom and the relative energies of stationary points obtained by CCSD(T)/aug-cc-pV(X+d)Z (X = D, T, Q and 5) agree reasonably well with each other. Therefore, the energies of all sampled points are calculated at the level of FC-UCCSD(T)-F12a/aug-cc-pVTZ,^{29,30} implemented by the software MOLPRO 2010.³² FC denotes “frozen-core” treatment in the post-Hartree-Fock calculations. Detailed comparisons of the energies and frequencies of the stationary points are given in Section IV A.

Sampling *ab initio* points is vital in developing a global PES to an acceptable degree of fidelity, without the need for unreasonable computational efforts. The strategy in this work is as follows. Atom centered density matrix propagation (ADMP) molecular dynamics is firstly performed using the spin-unrestricted Hartree-Fock method with the contracted Gaussian basis set 6-311G (UHF/6-311G) by Gaussian 09, Revision B.01.³³ The first batch of data points is selected from the ADMP trajectories and used to generate a raw PES. Due to the lack of data points, artificial wells in the raw PES will exist. Starting from the raw PES, a batch of trajectories is launched from different positions of the PES at different temperatures. New points whose geometries are not close to the existing dataset are selected and added to the dataset to patch up the unphysical regions of the PES. The closeness between any point \vec{r}_i' and an existing dataset \vec{r}_i is judged by the Euclidean distance defined in terms of the bond lengths, $\chi(\vec{r}_i) = \sqrt{\sum_{i=1}^{10} |\vec{r}_i - \vec{r}_i'|^2}$. χ is taken as 0.1 Å and the permutationally equivalent points are also included in such a

screening. The procedure is iterated many times and a new PES is fitted every time when new points are added to the dataset. Finally, a total of 82 680 points are retained in the dataset with an energy interval of 80 kcal mol⁻¹.

The fundamental invariant-neural network (FI-NN) method²⁸ is employed to fit the PES. The permutation invariance of the PES with respect to the identical atoms is enforced by introducing permutationally invariant polynomials (PIPs) to the neural network as inputs. Instead of using all PIPs truncated to a given order in the PIP-NN approach,^{34–36} the FI-NN method minimizes the number of input PIPs. The Morse-like variables, $P_{ij} = \exp(-r_{ij}/\alpha)$, are used to construct the polynomials with α as an adjustable constant and r_{ij} as the internuclear distance between the *i*th and *j*th atoms.^{37,38} α is taken as 1.2 Å. For the system A₃BC, there exist 20 fundamental invariants with a maximum degree of 3. The structure of the neural network is 20-50-80-1, which contains 20 invariant polynomials as inputs, 50 and 80 neurons in two hidden layers, and 1 output of potential energy, resulting in 5211 parameters. All fittings are performed using the Levenberg–Marquardt algorithm,^{39,40} and

the root mean square error (RMSE) defined as $\text{RMSE} =$

$\sqrt{\sum_{i=1}^{N_{\text{data}}} (E_{\text{fit}} - E_{\text{ab initio}})^2 / N_{\text{data}}}$ is used to assess the quality of the fitting. In each NN fitting, the dataset is randomly divided into two parts, 95% of the points as the training set and the rest, 5%, as the validating set. Only fits with similar RMSEs for the two sets are chosen to avoid false extrapolation. The final PES is taken as the average of three best fits with the training/validating/maximum RMSEs of 4.61/10.02/173.90, 5.16/12.15/87.53, and 6.06/10.17/226.10 meV, respectively. The so-called ensemble approach⁴¹ could minimize random errors. The overall RMSE of the PES is 4.72 meV.

III. Quasi-classical trajectory method

The integral cross section (ICS) of the reaction is computed by performing standard QCT calculations on the new PES, implemented by the software VENUS,³¹ according to

$$\sigma_r(E_c) = \pi b_{\text{max}}^2 \frac{N_r}{N_{\text{tot}}}, \quad (1)$$

where N_r and N_{tot} are the numbers of reactive and total trajectories at a specified collision energy E_c . The maximal impact parameter b_{max} is determined using small batches of trajectories with trial values at each specified initial state. The statistical error is given by $\Delta = \sqrt{(N_{\text{tot}} - N_r)/N_{\text{tot}}N_r}$.

The differential cross section (DCS) is obtained by

$$\frac{d\sigma_r}{d\Omega} = \frac{\sigma_r P_r(\theta)}{2\pi \sin(\theta)}, \quad (2)$$

where $P_r(\theta)$ is the normalized probability. The scattering angle θ is defined as

$$\theta = \cos^{-1} \left(\frac{|\vec{v}_i \cdot \vec{v}_f|}{|\vec{v}_i| |\vec{v}_f|} \right), \quad (3)$$

in which $\bar{v}_i = \bar{v}_{\text{OH}} - \bar{v}_{\text{H}_2\text{S}}$ and $\bar{v}_f = \bar{v}_{\text{H}_2\text{O}} - \bar{v}_{\text{SH}}$ denote the initial and final relative velocities.

The rate coefficient at temperature T is calculated by

$$k(T) = \frac{1}{Q_e} \left(\frac{8k_B T}{\pi \mu} \right)^{1/2} \pi b_{\text{max}}^2 \frac{N_f}{N_i}, \quad (4)$$

where μ is the reduced mass between the reactants OH and H₂S and k_B is the Boltzmann constant. The electronic partition function Q_e is obtained by $(2 + 2e^{-140/k_B T})/2$, in which the spin-orbit splitting of OH is taken as 140 cm⁻¹.⁴² At each specific temperature T , the initial ro-vibrational energies of the two reactants and the collision energy are sampled according to the Boltzmann distribution.

The vibrational state distribution of the product SH is determined by the Einstein–Brillouin–Keller semiclassical quantization of the action integral. While for the triatomic product H₂O, the quantization is not straightforward. The NMA approach developed by Corchado and Espinosa–García^{43–47} is adopted to assign quantum-like vibrational states. Unlike the traditional scheme extracting the coordinates and momenta from the last step of each trajectory, they are taken from a specific step of each reactive trajectory within the last vibrational period of the product molecule. The step is determined by demanding that the corresponding geometry has a minimum potential energy.⁴⁸ Test calculations showed that the new scheme works much better than the traditional one. Detailed information can be found in ref. 49.

In mode-specific dynamics calculations, the initial vibrational states of H₂S are sampled using the fixed normal mode method and the initial states of OH are sampled using the conventional semi-classical method. The reactants are both located in the rotational ground state. 20 000–100 000 trajectories are run for each initial state with the collision energy ranging from 3 kcal mol⁻¹ to 25 kcal mol⁻¹, resulting in statistical errors of below 3%. In kinetics calculations, ~250 000 trajectories are dispatched at each temperature. The trajectories are launched from a reactant separation of 8.5 Å and ended when products or reactants reach a separation of 9.0 Å for reactive or non-reactive trajectories. The time step is taken as 0.05 fs, guaranteeing a convergence of total energy better than 10⁻³ kcal mol⁻¹ in the propagation.

IV. Results and discussion

A. Properties of the potential energy surface

The schematic diagram of the reaction path is illustrated in Fig. 1. The *ab initio* energies at the level of UCCSD(T)-F12a/aug-cc-pVTZ and the values of the fitted PES and ZPE corrected potential energies of all stationary points are listed below the corresponding geometries with respect to the reactant asymptote. There exist two minima in both the entrance valley and the exit valley, in which RC-A and PC-A refer to hydrogen-bonded complexes while RC-B and PC-B correspond to hemibonded complexes. They all belong to the state ²A' and the hydrogen-bonded complex is slightly more stable than the associated

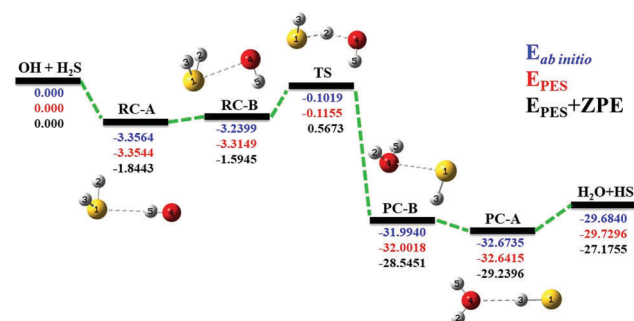


Fig. 1 Schematic diagram of the reaction path for the OH + H₂S → H₂O + SH reaction. The *ab initio* energies of stationary points at the level of UCCSD(T)-F12a/aug-cc-pVTZ, the values of the fitted PES and the zero-point energy corrected values are shown below the corresponding geometries. All energies are given in kcal mol⁻¹ and relative to the reactant asymptote.

hemibonded complex, in accord with Tang *et al.*'s calculations.²⁷ However, another hydrogen-bonded isomer with the symmetry of ²A'' was reported by Tang *et al.* in both the entrance and exit channels, whose energy is higher than the others by less than 1.6 kcal mol⁻¹.²⁷

Table 1 lists the optimized geometries of the stationary points at the level of UCCSD(T)-F12a/aug-cc-pVTZ, the geometries on the fitted PES and available experimental values. Tang *et al.*'s results at the level of CCSD(T)/aug-cc-pV(Q+d)Z are also presented for comparison.²⁷ It can be seen that the geometries by UCCSD(T)-F12a/aug-cc-pVTZ agree well with the counterparts by CCSD(T)/aug-cc-pV(Q+d)Z with the bond length difference being less than 0.052 Å and the angle difference being less than 2.3°. On the other hand, the PES reproduces well the *ab initio* geometries. The bond lengths differ by less than 0.064 Å and the angles differ by less than 10°. The energies and harmonic frequencies of the stationary points are given in Table 2. The fitted values are in good accordance with the *ab initio* results obtained by using UCCSD(T)-F12a/aug-cc-pVTZ. The energy difference is less than 0.075 kcal mol⁻¹ and the frequency difference is less than 54 cm⁻¹. The large difference generally occurs for the shallow wells. Two points should be pointed out here. On one side, the barrier height on the fitted PES is -0.1155 kcal mol⁻¹, indicating the reaction is a barrierless reaction. This is in contrast to the value of 0.06 eV obtained by using CCSD(T)/aug-cc-pV(Q+d)Z although the absolute error is not large.²⁷ On the other side, the complex PC-A has an imaginary frequency of 53i cm⁻¹ in the fitted PES, which is consistent with our *ab initio* calculation of 58i cm⁻¹ obtained by using UCCSD(T)-F12a/aug-cc-pVTZ. However, Tang *et al.*²⁷ predicted a value of 30 cm⁻¹ by using CCSD(T)/aug-cc-pV(Q+d)Z. These discrepancies are believed to have negligible effects on the reaction dynamics calculations.

Fig. 2 depicts the contours of the PES as a function of the bond lengths of the breaking SH and the forming OH with the other coordinates fixed at the geometry of the transition state. Obviously, the smoothness of the PES is very good. There exists a small bump in the entrance valley, resulting from the other reaction channel H₂S + OH → HSOH + H. This channel is an

Table 1 Geometries (length in angstrom and angle in degree) of the stationary points for the OH + H₂S → H₂O + SH reaction. The corresponding atom labels are shown in Fig. 1

Species	Method	$R_{S_1H_2}$	$R_{S_1H_3}$	$R_{H_2O_4}$	$R_{O_4H_5}$	$\theta_{H_2S_1H_3}$	$\theta_{S_1H_2O_4}$	$\theta_{H_2O_4H_5}$	$\phi_{H_3S_1H_2O_4}$	$\phi_{S_1H_2O_4H_5}$
OH	<i>Ab initio</i> ^a				0.970					
	<i>Ab initio</i> ^b				0.970					
	PES ^c				0.971					
	Expt. ^d				0.970					
H ₂ S	<i>Ab initio</i> ^a	1.339				92.4				
	<i>Ab initio</i> ^b	1.338				92.4				
	PES ^c	1.339				92.3				
	Expt. ^d	1.336				92.1				
RC-A	<i>Ab initio</i> ^a	1.340	1.340	3.827	0.975	92.5	65.2	23.0	94.6	6.4
	<i>Ab initio</i> ^b	1.340	1.340	3.819	0.975	92.5	65.5	23.2	94.2	6.8
	PES ^c	1.340	1.340	3.871	0.975	92.5	63.4	19.1	96.8	-3.6
RC-B	<i>Ab initio</i> ^a	1.339	1.339	2.624	0.969	92.6	76.5	105.9	72.7	51.2
	<i>Ab initio</i> ^b	1.338	1.338	2.631	0.969	92.6	76.1	106.0	73.2	51.2
	PES ^c	1.338	1.338	2.666	0.969	92.4	75.1	106.1	74.6	50.7
TS	<i>Ab initio</i> ^a	1.401	1.340	1.488	0.970	92.1	136.5	102.4	71.0	39.2
	<i>Ab initio</i> ^b	1.402	1.339	1.483	0.970	92.2	137.5	102.4	70.8	38.6
	PES ^c	1.402	1.341	1.489	0.971	92.2	134.5	102.9	70.8	41.8
PC-A	<i>Ab initio</i> ^a	4.182	1.347	0.959	0.959	10.7	42.1	105.0	0.0	180.0
	<i>Ab initio</i> ^b	4.185	1.346	0.959	0.959	10.5	42.0	104.9	0.0	180.0
	PES ^c	4.197	1.347	0.959	0.959	10.4	42.0	104.9	0.0	180.0
PC-B	<i>Ab initio</i> ^a	3.366	1.341	0.960	0.960	74.7	62.1	104.7	-49.4	-105.3
	<i>Ab initio</i> ^b	3.418	1.340	0.960	0.960	72.8	61.0	104.6	-49.3	-107.6
	PES ^c	3.302	1.341	0.960	0.960	78.2	62.8	104.8	-49.7	-104.0
SH	<i>Ab initio</i> ^a	1.343								
	<i>Ab initio</i> ^b	1.342								
	PES ^c	1.343								
	Expt. ^d	1.341								
H ₂ O	<i>Ab initio</i> ^a				0.959			104.4		
	<i>Ab initio</i> ^b				0.958			104.4		
	PES ^c				0.959			104.5		
	Expt. ^d				0.958			104.5		

^a This work, UCCSD(T)-F12a/aug-cc-pVTZ by Molpro 2010. ^b CCSD(T)/aug-cc-pV(Q+d)Z by CFOUR, see ref. 27. ^c This work, FI-NN PES. ^d See <http://cccbdb.nist.gov>.

endothermic reaction and has a barrier height of ~ 20 kcal mol⁻¹. Since we are only interested in the hydrogen abstraction channel in this work, the product channel of HSOH and H is not covered in the PES.

B. Mode-specific dynamics

Fig. 3 shows the mode-specific total ICSs of the OH + H₂S → H₂O + SH reaction as a function of collision energy. Both reactants are in their ground rotational states. The initial vibrational states are labelled (ν_{OH} ; ν_1 , ν_2 and ν_3), in which ν_{OH} denotes the quantum number of the OH vibrational mode, and ν_1 , ν_2 , and ν_3 represent the quantum numbers of the symmetric stretching mode, the bending mode, and the anti-symmetric stretching mode, respectively. It can be seen that firstly, the ICS from the ground state increases monotonically from an energy threshold of below 2 kcal mol⁻¹ with the collision energy, predicting a positive reaction barrier. This agrees with the ZPE corrected barrier height of 0.5673 kcal mol⁻¹ on the PES. Secondly, exciting the symmetric stretching mode or the

asymmetric stretching mode of the reactant H₂S significantly enhances the reaction. It is noteworthy that the promotional effects of exciting the two stretching modes are nearly the same over the energy range studied. Actually, the equivalence between the symmetric and asymmetric stretching modes in promoting a reaction has been reported in the H + H₂S and H + NH₃ reactions,^{50–52} and it is partially attributed to the strong local mode character of the reactants. Thirdly, exciting the bending mode of H₂S promotes the reaction but its efficiency is not as high as that of the stretching modes. It appears that the promotional effect increases with the collision energy. Besides, the vibrational energy initially deposited in the OH bond has a negligible effect on the reaction, indicating that OH is a good spectator bond.

To unveil the reaction mechanisms of the OH + H₂S → H₂O + SH reaction, Fig. 4 presents the DCSS from the ground states of the reactants with collision energies of 3, 5, 8, 10, 12, 15, 20 and 25 kcal mol⁻¹. At low collision energies, the products are almost isotropically scattered, indicating that the indirect mechanism

Table 2 Energies (in kcal mol⁻¹) and harmonic frequencies (in cm⁻¹) of the stationary points for the OH + H₂S → H₂O + SH reaction

Frequency (cm ⁻¹)											
Species	Method	<i>E</i> (kcal mol ⁻¹)	1	2	3	4	5	6	7	8	9
H ₂ S + OH	<i>Ab initio</i> ^a	0.0000	3738	2736	2720	1212					
	<i>Ab initio</i> ^b	0.0000	3739	2738	2722	1212					
	PES ^c	0.0000	3740	2727	2719	1210					
	Expt. ^d		3738	2626	2615	1183					
RC-A	<i>Ab initio</i> ^a	-3.3564	3648	2731	2715	1209	443	329	139	137	103
	<i>Ab initio</i> ^b	-3.31	3654	2734	2719	1210	440	330	139	136	111
	PES ^c	-3.3544	3658	2724	2701	1208	389	363	156	145	117
RC-B	<i>Ab initio</i> ^a	-3.2399	3755	2737	2723	1206	479	264	252	92	70
	<i>Ab initio</i> ^b	-3.11	—	—	—	—	—	—	—	—	—
	PES ^c	-3.3149	3746	2731	2707	1184	483	278	266	126	87
TS	<i>Ab initio</i> ^a	-0.1019	3743	2722	1808	1112	717	320	255	181	865i
	<i>Ab initio</i> ^b	0.06	3744	2725	1786	1112	721	326	258	181	871i
	PES ^c	-0.1155	3749	2715	1805	1114	716	328	265	192	915i
PC-A	<i>Ab initio</i> ^a	-32.6735	3942	3833	2670	1645	350	192	110	56	58i
	<i>Ab initio</i> ^b	-32.47	3939	3830	2675	1648	347	195	109	74	30
	PES ^c	-32.6415	3938	3823	2666	1645	308	211	106	88	53i
PC-B	<i>Ab initio</i> ^a	-31.9940	3933	3823	2714	1645	229	144	130	92	64
	<i>Ab initio</i> ^b	-31.71	—	—	—	—	—	—	—	—	—
	PES ^c	-32.0018	3930	3822	2709	1656	243	164	158	77	63
SH + H ₂ O	<i>Ab initio</i> ^a	-29.6840	3942	3832	2696	1646					
	<i>Ab initio</i> ^b	-29.51	3941	3831	2700	1650					
	PES ^c	-29.7296	3946	3833	2694	1646					
	Expt. ^d		3756	3657	2696	1595					

^a This work, UCCSD(T)-F12a/aug-cc-pVTZ by Molpro 2010. ^b CCSD(T)/aug-cc-pV(Q+d)Z by CFOUR, see ref. 27. ^c This work, FI-NN PES. ^d See <http://cccbdb.nist.gov>.

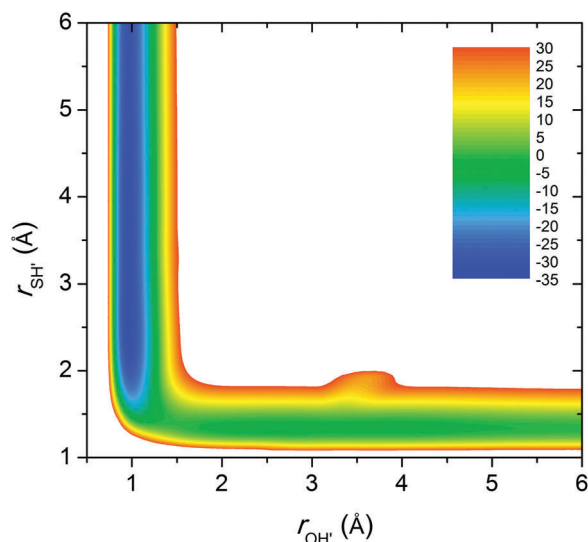


Fig. 2 Contours of the PES as a function of bond lengths of the breaking SH and the forming OH with all other coordinates optimized. The energy is taken from -35 to 30 kcal mol⁻¹ with an interval of 1.25 kcal mol⁻¹.

dominates the reaction, because the colliders are trapped in the pre- or post-reaction wells. When the collision energy increases, the direct mechanism becomes more and more prevalent. In the moderate collision energy range from 8.0 to 15.0 kcal mol⁻¹, the

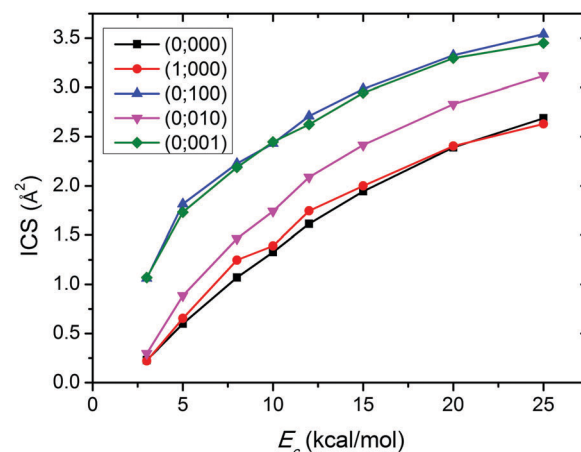


Fig. 3 Integral cross sections of the OH + H₂S → H₂O + SH reaction as a function of collision energy. The numbers (*v*_{OH}; *v*₁, *v*₂, *v*₃) in parenthesis denote excitations in the OH vibration, the symmetric stretching mode, the bending mode and the asymmetric stretching mode of H₂S, respectively.

reaction starts to favor backward and sideways scattering. As the collision energy increases further, the reaction prefers forward scattering to backward and sideways scattering although the latter two still have significant contributions. By analyzing the correlation between the impact parameter and the scattering angle, the forward scattering results from large impact parameter collisions

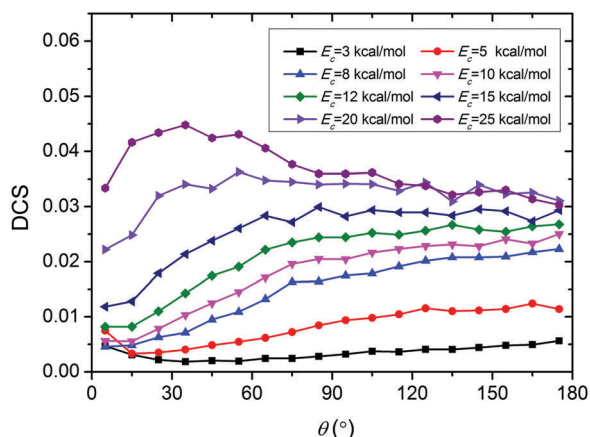


Fig. 4 Differential cross sections of the $\text{OH} + \text{H}_2\text{S} \rightarrow \text{H}_2\text{O} + \text{SH}$ reaction from the reactant ground states with collision energies of 3, 5, 8, 10, 12, 15, 20 and 25 kcal mol^{-1} .

while the backward scattering is correlated to small impact parameter collisions. Therefore, the forward scattering arises from the stripping mechanism and the backward scattering is caused by the rebound mechanism.

C. Final-state distribution

State-to-state dynamics could provide a comprehensive understanding of chemical reactions. There is always hope that in dynamics studies, one can unveil how different kinds of energy are redistributed. Fig. 5 and 6 plot the vibrational state distributions of the products H_2O and SH from the reactant ground states, the fundamentals of the symmetric and asymmetric stretching modes of H_2S and the fundamental of the OH vibrational mode. The collision energy is 8 and 20 kcal mol^{-1} . Two binning methods, histogram binning (HB) and energy-based Gaussian binning (1GB),^{46,53} are implemented in the calculations. It can be seen that the HB and 1GB methods give similar results. Therefore, the following discussions are based on the 1GB results.

From the reactant ground states with $E_c = 8 \text{ kcal mol}^{-1}$, the product H_2O is largely distributed in the states (002) and (200), followed by the states (210), (300) and (012). The population in the ground state is negligible. The inverted vibrational state distribution of the product H_2O is partially attributed to the elongated bond length of OH . As shown in Table 1, the bond length of the forming OH is elongated to 1.489 Å, compared to 0.959 Å in the product H_2O . As the collision energy increases to 20 kcal mol^{-1} , the populations of the product H_2O in the states

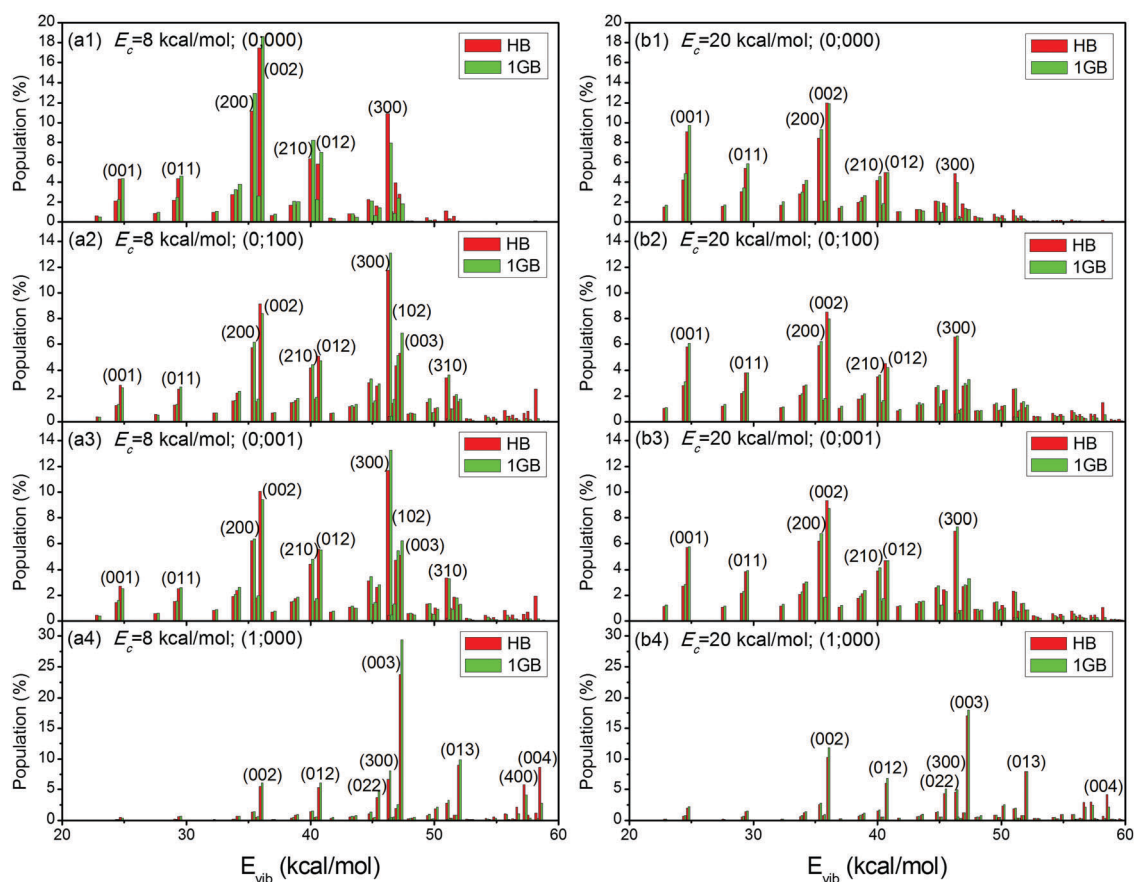


Fig. 5 Vibrational state distributions of the product H_2O from the reactant ground state (upper, labeled 1), the fundamental states of the symmetric stretching mode (middle, labeled 2) and the asymmetric stretching mode (middle, labeled 3) of H_2S , and the OH vibration mode (lower, labeled 4) at $E_c = 8$ (left, denoted as a) and 20 (right, denoted as b) kcal mol^{-1} . Two binning methods, HB and 1GB, are color coded as red and green, respectively.

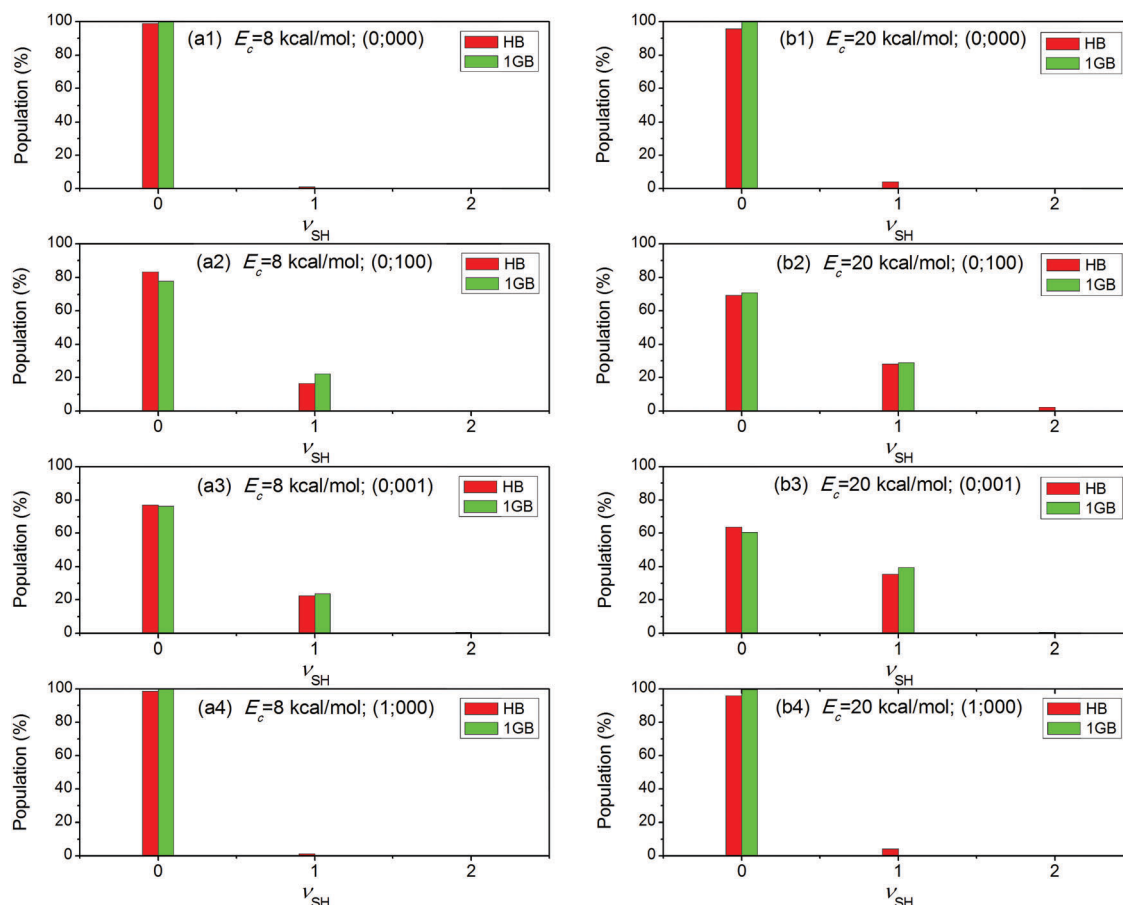


Fig. 6 Vibrational state distributions of the product SH from the reactant ground state (upper, labeled 1), the fundamental states of the symmetric stretching mode (middle, labeled 2) and the asymmetric stretching mode (middle, labeled 3) of H_2S , and the OH vibration mode (lower, labeled 4) at $E_c = 8$ (left, denoted as a) and 20 (right, denoted as b) kcal mol^{-1} . Two binning methods, HB and 1GB, are color coded as red and green, respectively.

Table 3 Comparison of the theoretical and experimental vibrational distribution of the product H_2O from the $\text{OH} + \text{H}_2\text{S} \rightarrow \text{H}_2\text{O} + \text{SH}$ reaction

$\nu_{1,3}^a$	ν_2			1			2		
	Theo1 ^b	Theo2 ^c	Exp. ^d	Theo1 ^b	Theo2 ^c	Exp. ^d	Theo1 ^b	Theo2 ^c	Exp. ^d
0	0.14	1.48	2.6	0.39	1.34	4.5	0.52	1.69	3.6
1	6.61	14.58	10.3	7.08	9.31	17.7	7.08	7.16	14.3
2	34.14	23.36	24.4	17.49	11.41	20.6	4.2	4.57	0.8
3	13.03	7.07	4.5	0.36	1.35			0.18	

^a $\nu_{1,3} = \nu_1 + \nu_3$. ^b Theo1 denotes the calculated distribution from the reactant ground states with $E_c = 8 \text{ kcal mol}^{-1}$. ^c Theo2 denotes the calculated distribution from the reactant ground states with $E_c = 20 \text{ kcal mol}^{-1}$. ^d Exp. denotes the measured vibrational distribution from the room-temperature reaction at a pressure of 0.5 Torr, see ref. 24.

(002) and (200) decline while the population in the state (001) increases. This means that increasing the collision energy cannot effectively increase the vibrational energy of the product H_2O . Exciting either the symmetric stretching mode or the asymmetric stretching mode gives nearly the same vibrational state distribution of H_2O . Compared with the distribution from the ground states, the populations in the states (300), (102), (201) and (003) slightly increase while the populations in the states (200) and (002) decrease. Therefore, exciting the symmetric stretching mode of H_2S brings about similar dynamical

behavior to exciting the asymmetric stretching mode even at the state-to-state level. And, only a small part of the vibrational energy deposited in the stretching modes of H_2S flows into the vibrational modes of H_2O . When the reactant OH is vibrationally excited, the product H_2O is dominated in the state (003) at $E_c = 8 \text{ kcal mol}^{-1}$ and becomes slightly decentralized at $E_c = 20 \text{ kcal mol}^{-1}$.

The product SH is exclusively distributed in the ground state when the reactants are unexcited. Exciting the reactant OH has no effect on the vibrational distribution of SH. However, when

either the symmetric stretching mode or the asymmetric stretching mode is fundamentally excited, a significant portion of the vibrational energy is preserved in the SH bond.

Table 3 compares the calculated vibrational distribution of the product H_2O with the experimental result of Butkovskaya and Setser.²⁴ The vibrational distribution of H_2O was measured from the room-temperature reaction at a total pressure of 0.5 Torr. At room temperature, the reactants are expected to be mainly populated in the vibrational ground states. However, it is difficult to estimate the relative velocity of the reactants from a total pressure. Thus, the theoretical distributions at $E_c = 8 \text{ kcal mol}^{-1}$ and 20 kcal mol^{-1} are both listed in the table. In the experiment, the symmetric stretching mode and the asymmetric stretching mode of the product H_2O were not distinguished. Therefore, the notation $\nu_{1,3}$ means the sum of ν_1 and ν_3 . It can be seen that the product H_2O for $\nu_2 = 0, 1$ and 2 presents an inverted distribution associated with $\nu_{1,3}$, in agreement with the experimental distribution. Its largest population is in the states with $\nu_{1,3} = 2$ for $\nu_2 = 0$ and 1 and with $\nu_{1,3} = 1$ for $\nu_2 = 2$. Interestingly, the theoretical distribution of $\nu_{1,3}$ at $E_c = 20 \text{ kcal mol}^{-1}$ agrees well with the experimental distribution under the condition that $\nu_2 = 0$. This suggests that the reactants in the experiment possibly have relatively high collision energies. In addition, the visible discrepancy for $\nu_2 = 1$ and 2 may be caused by the inherent defect of the NMA method in analyzing combination band excitations⁴⁹ and the different initial conditions.

The product energy partitioning in the $\text{OH} + \text{H}_2\text{S} \rightarrow \text{H}_2\text{O} + \text{SH}$ reaction is shown in Fig. 7, where $f_v(\text{H}_2\text{O})$, $f_r(\text{H}_2\text{O})$, $f_v(\text{SH})$, $f_r(\text{SH})$ and f_t are the fractions of the available energy released as the vibrational energy of H_2O , the rotational energy of H_2O , the vibrational energy of SH, the rotational energy of SH and the relative translational energy. On one hand, most of the available energy is released as the vibrational energy of H_2O ,

followed by the product translational energy and the rotational energy of H_2O . On the other hand, at a specific collision energy, $f_r(\text{H}_2\text{O})$, $f_r(\text{SH})$ and f_t are nearly independent of the initial states. When the collision energy increases from 8 kcal mol^{-1} to 20 kcal mol^{-1} , f_t is almost doubled while $f_v(\text{H}_2\text{O})$ significantly decreases. Thus, most of the reactant collision energy converts to the product translational energy. This can be easily understood considering that the dominant reaction mechanism changes from the indirect mechanism to the direct mechanism. In direct rebounding and stripping mechanisms, the available energy flows into the product translational mode more, boosting the products to depart from each other. When either the symmetric stretching mode or the asymmetric stretching mode of H_2S is fundamentally excited, $f_r(\text{SH})$ slightly increases although the overall fraction is small. Besides, most of the energy initially deposited in the OH vibrational mode converts to the vibrational energy of the product H_2O . Furthermore, the experimentally measured $f_v(\text{H}_2\text{O})$ is 58%,²⁴ in good accordance with the calculated fraction of 55.84% from the reactant ground states at $E_c = 20 \text{ kcal mol}^{-1}$.

D. Non-Arrhenius behavior

Non-Arrhenius behavior in chemical reactions has attracted considerable attention.⁵⁴ The calculated rate constants of the $\text{OH} + \text{H}_2\text{S} \rightarrow \text{H}_2\text{O} + \text{SH}$ reaction at 1500, 800, 500 and 350 K are 2.97×10^{-11} , 9.92×10^{-12} , 5.84×10^{-12} and $2.48 \times 10^{-12} \text{ cm}^3 \text{ molecule}^{-1} \text{ s}^{-1}$, respectively. They are plotted in Fig. 8 together with the earlier experimental values. Obviously, there exists an unusual temperature dependence of the rate constants. The unusual temperature dependence at high temperatures can be attributed to the strong vibrational mode specificity. The calculated rate constant at 800 K agrees well with the experimental value of $1.34 \times 10^{-11} \text{ cm}^3 \text{ molecule}^{-1} \text{ s}^{-1}$.⁹ At 500 K, a theoretical rate constant of $5.84 \times 10^{-12} \text{ cm}^3 \text{ molecule}^{-1} \text{ s}^{-1}$ is in between

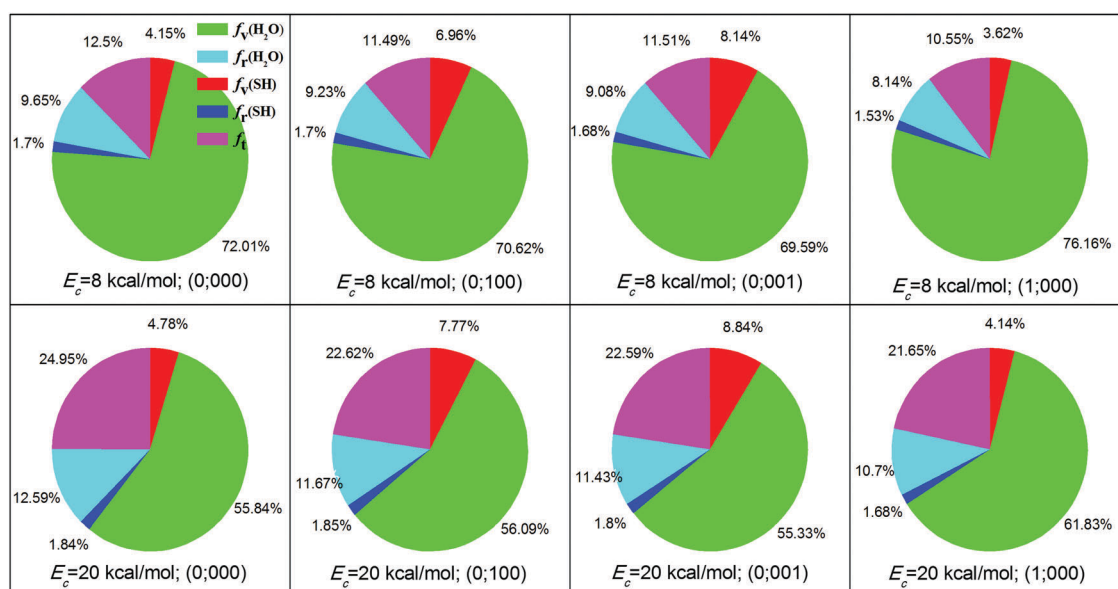


Fig. 7 Product energy disposal from different initial states at $E_c = 8$ (upper) and 20 (lower) kcal mol^{-1} .

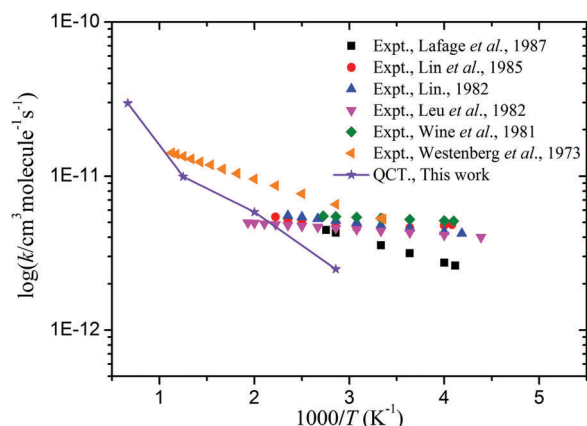


Fig. 8 Comparison of the calculated and measured thermal rate constants for the $\text{OH} + \text{H}_2\text{S} \rightarrow \text{H}_2\text{O} + \text{SH}$ reaction.

the two experimental values of 4.95×10^{-12} and $9.59 \times 10^{-12} \text{ cm}^3 \text{ molecule}^{-1} \text{ s}^{-1}$.^{9,21} In contrast, the calculated rate constant at 350 K is visibly lower than the experimental values. This is partly caused by the neglect of the quantum tunneling effect in the QCT calculations, which generally plays an important role at low temperatures. It is our plan to perform mode-specific quantum scattering calculations (possibly using a reduced-dimensional model due to the existence of two heavy atoms) on the PES to clarify the origin of the Non-Arrhenius behavior at low temperatures.

V. Conclusions

An accurate full-dimensional global PES of the $\text{OH} + \text{H}_2\text{S} \rightarrow \text{H}_2\text{O} + \text{SH}$ reaction is developed by fitting a total of 82 680 *ab initio* points sampled in the relevant configurational space at the level of UCCSD(T)-F12a/aug-cc-pVTZ. The flexible FI-NN method is employed in the fitting, resulting in a RMSE of 4.72 meV. The properties of the stationary points, including geometries, energies and harmonic frequencies, are well reproduced by the new PES.

QCT calculations are carried out on the PES to study the mode-specific dynamics. Exciting either the symmetric stretching mode or the asymmetric stretching mode of H_2S significantly promotes the reactivity with nearly the same efficiency. Exciting the bending mode slightly enhances the reaction at low collision energies while the promotional effect increases with the collision energy. Besides, the reactant OH acts as a good spectator.

The vibrational state distributions of the products H_2O and SH are calculated using the NMA method. The obtained vibrational state distribution of H_2O agrees reasonably well with the earlier experimental results. The product H_2O has an inverted vibrational state distribution, which is attributed to the elongated bond length of OH at the transition state. The product SH is dominantly distributed in the ground state. The product energy partitioning in the reaction indicates that most of the available energy is released as the vibrational energy of H_2O ,

followed by the product translational energy and the rotational energy of H_2O .

There exists a non-Arrhenius temperature dependence of the rate constants of the reaction. The calculated rate constants at 800 and 500 K are in good accord with the experimental values. However, due to the neglect of the quantum tunneling effect, the calculated rate at 350 K is visibly lower than the experimental value.

Conflicts of interest

There are no conflicts to declare.

Acknowledgements

This work is supported by the National Natural Science Foundation of China (Grant No. 21603266 to HS and 21773297 to MY).

References

- 1 C. F. Cullis and M. M. Hirschler, *Atoms. Environ.*, 1980, **14**, 1263–1278.
- 2 D. Möller, *Atoms. Environ.*, 1984, **18**, 19–27.
- 3 D. R. Hitchcock, *J. Air Pollut. Control Assoc.*, 1976, **26**, 210–215.
- 4 T. E. Graedel, *Rev. Geophys.*, 1977, **15**, 421–428.
- 5 R. O. Beauchamp, J. S. Bus, J. A. Popp, C. J. Boreiko, D. A. Andjelkovich and P. Leber, *CRC Crit. Rev. Toxicol.*, 1984, **13**, 25–97.
- 6 W. Jaeschke, H. Claude and J. Herrmann, *J. Geophys. Res.: Oceans*, 1980, **85**, 5639–5644.
- 7 M. Frenklach, J. H. Lee, J. N. White and W. C. Gardiner, *Combust. Flame*, 1981, **41**, 1–16.
- 8 I. A. Gargurevich, *Ind. Eng. Chem. Res.*, 2005, **44**, 7706–7729.
- 9 A. A. Westenberg and N. deHaas, *J. Chem. Phys.*, 1973, **59**, 6685–6686.
- 10 R. A. Perry, R. Atkinson and J. N. Pitts, *J. Chem. Phys.*, 1976, **64**, 3237–3239.
- 11 P. H. Wine, N. M. Kreutter, C. A. Gump and A. R. Ravishankara, *J. Phys. Chem.*, 1981, **85**, 2660–2665.
- 12 C. L. Lin, *Int. J. Chem. Kinet.*, 1982, **14**, 593–598.
- 13 Y.-L. Lin, N.-S. Wang and Y.-P. Lee, *Int. J. Chem. Kinet.*, 1985, **17**, 1201–1214.
- 14 C. Lafage, J.-F. Pauwels, M. Carlier and P. Devolder, *J. Chem. Soc., Faraday Trans. 2*, 1987, **83**, 731–739.
- 15 H. Wang, D. Zhu, W. Wang and Y. Mu, *Chin. Sci. Bull.*, 2010, **55**, 2951–2955.
- 16 C. Wilson and D. M. Hirst, *J. Chem. Soc., Faraday Trans.*, 1994, **90**, 3051–3059.
- 17 S. H. Mousavipour, M. A. Namdar-Ghanbari and L. Sadeghian, *J. Phys. Chem. A*, 2003, **107**, 3752–3758.
- 18 B. A. Ellingson and D. G. Truhlar, *J. Am. Chem. Soc.*, 2007, **129**, 12765–12771.
- 19 B. Du and W. Zhang, *Comput. Theor. Chem.*, 2015, **1069**, 77–85.
- 20 R. A. Cox and D. Sheppard, *Nature*, 1980, **284**, 330.

- 21 M.-T. Leu and R. H. Smith, *J. Phys. Chem.*, 1982, **86**, 73–81.
- 22 J. V. Michael, D. F. Nava, W. D. Brobst, R. P. Borkowski and L. J. Stief, *J. Phys. Chem.*, 1982, **86**, 81–84.
- 23 I. Barnes, V. Bastian, K. H. Becker, E. H. Fink and W. Nelsen, *J. Atmos. Chem.*, 1986, **4**, 445–466.
- 24 N. I. Butkovskaya and D. W. Setser, *J. Phys. Chem. A*, 1998, **102**, 6395–6405.
- 25 B. Wang, H. Hou and Y. Gu, *J. Mol. Struct.: THEOCHEM*, 2000, **505**, 241–246.
- 26 B. Alday, R. Johnson, J. Li and H. Guo, *Theor. Chem. Acc.*, 2014, **133**, 1540.
- 27 M. Tang, X. Chen, Z. Sun, Y. Xie and H. F. Schaefer, *J. Phys. Chem. A*, 2017, **121**, 9136–9145.
- 28 K. Shao, J. Chen, Z. Zhao and D. H. Zhang, *J. Chem. Phys.*, 2016, **145**, 071101.
- 29 T. B. Adler, G. Knizia and H.-J. Werner, *J. Chem. Phys.*, 2007, **127**, 221106.
- 30 G. Knizia, T. B. Adler and H.-J. Werner, *J. Chem. Phys.*, 2009, **130**, 054104.
- 31 W. L. Hase, R. J. Duchovic, X. Hu, A. Komornicki, K. F. Lim, D.-H. Lu, G. H. Peslherbe, K. N. Swamy, S. R. V. Linde, A. Varandas, H. Wang and R. J. Wolf, *Quantum Chem. Program Exch. Bull.*, 1996, **16**, 671.
- 32 P. J. K. H.-J. Werner, G. Knizia, F. R. Manby and M. Schütz, *et al.*, *MOLPRO, version 2010.1, a package of ab initio programs*, 2010, see <http://www.molpro.net>.
- 33 M. J. Frisch, G. W. Trucks, H. B. Schlegel, G. E. Scuseria, M. A. Robb, J. R. Cheeseman, G. Scalmani, V. Barone, G. A. Petersson, H. Nakatsuji and X. M. Li, *et al.*, *Gaussian 09, Revision B.01*, Gaussian, Inc., Wallingford CT, 2009.
- 34 B. Jiang and H. Guo, *J. Chem. Phys.*, 2013, **139**, 054112.
- 35 J. Li, B. Jiang and H. Guo, *J. Chem. Phys.*, 2013, **139**, 204103.
- 36 B. Jiang and H. Guo, *J. Chem. Phys.*, 2014, **141**, 034109.
- 37 B. J. Braams and J. M. Bowman, *Int. Rev. Phys. Chem.*, 2009, **28**, 577–606.
- 38 Z. Xie and J. M. Bowman, *J. Chem. Theory Comput.*, 2009, **6**, 26–34.
- 39 M. T. Hagan and M. B. Menhaj, *IEEE Trans. Neural Networks*, 1994, **5**, 989–993.
- 40 L. M. Raff, R. Komanduri, M. Hagan and S. T. S. Bukkapatnam, *Neural Networks in Chemical Reaction Dynamics*, Oxford University Press, Oxford, 2012.
- 41 Z.-H. Zhou, J. Wu and W. Tang, *Artif. Intell.*, 2002, **137**, 239–263.
- 42 G. Herzberg, *J. Phys. Chem.*, 1940, **44**, 954.
- 43 J. Espinosa-García, J. L. Bravo and C. Rangel, *J. Phys. Chem. A*, 2007, **111**, 2761–2771.
- 44 J. Espinosa-García and J. L. Bravo, *J. Phys. Chem. A*, 2008, **112**, 6059–6065.
- 45 J. C. Corchado and J. Espinosa-Garcia, *Phys. Chem. Chem. Phys.*, 2009, **11**, 10157–10164.
- 46 G. Czako and J. M. Bowman, *J. Chem. Phys.*, 2009, **131**, 244302.
- 47 J. Li, J. C. Corchado, J. Espinosa-Garcia and H. Guo, *J. Chem. Phys.*, 2015, **142**, 084314.
- 48 Y. Zhu, L. Ping, M. Bai, Y. Liu, H. Song, J. Li and M. Yang, *Phys. Chem. Chem. Phys.*, 2018, **20**, 12543–12556.
- 49 L. Ping, L. Tian, H. Song and M. Yang, *J. Phys. Chem. A*, 2018, **122**, 6997–7005.
- 50 H. Song, M. Yang and H. Guo, *J. Chem. Phys.*, 2016, **145**, 131101.
- 51 J. Qi, D. Lu, H. Song, J. Li and M. Yang, *J. Chem. Phys.*, 2017, **146**, 124303.
- 52 H. Song and M. Yang, *Phys. Chem. Chem. Phys.*, 2018, **20**, 19647–19655.
- 53 G. Czako, *J. Phys. Chem. A*, 2012, **116**, 7467–7473.
- 54 I. W. M. Smith, *Chem. Soc. Rev.*, 2008, **37**, 812–826.